Materials Advances

ROYAL SOCIETY OF CHEMISTRY

PAPER

View Article Online
View Journal | View Issue

Check for updates

Cite this: *Mater. Adv.*, 2025, 6, 849

Thermoelectric performance of Bi-based novel Janus monolayer structures†

KM Sujata,[ab] Nidhi Verma,[a] Rekha Garg Solanki*[b] and Ashok Kumar *[a]

This work systematically investigates the stability and electronic and thermoelectric characteristics of newly discovered 2D Janus monolayers BiYZ (Y ≠ Z = Te, Se and S) according to the first-principles theory. Janus BiYZ monolayers are stable based on the AIMD simulations, positive phonon spectra plots and the evaluation of elastic strain tensor. These monolayers show a high carrier mobility (~10^3 cm^2 V^{-1} s^{-1}) and an indirect bandgap nature. The Janus monolayers BiTeSe, BiTeS and BiSeS show an ultralow lattice thermal conductivity of 0.04 W m^{-1} K^{-1}, 0.20 W m^{-1} K^{-1} and 0.02 W m^{-1} K^{-1}, respectively, at room temperature. Low lattice thermal conductivity is obtained due to a small phonon group velocity, high Grüneisen parameter, small phonon relaxation time and significantly reduced phonon transport. The maximum *ZT* values at 500 K reach up to 0.97, 0.60 and 1.78 for BiTeSe, BiSeS, and BiTeS monolayers, respectively. Our results suggest Janus BiYZ monolayers to be promising thermoelectric candidates due to their superior thermal and electrical transport characteristics and subsequent strong thermoelectric performance.

Received 12th September 2024,
Accepted 12th December 2024

DOI: 10.1039/d4ma00924j

rsc.li/materials-advances

Open Access Article. Published on 24 December 2024. Downloaded on 2/15/2026 7:07:25 PM.
This article is licensed under a Creative Commons Attribution-NonCommercial 3.0 Unported Licence.

1. Introduction

Currently, there is a severe energy shortage issue in our society.[1] Resources like coal and gas are running low, and they might be completely used up by 2050. Thus, there is a demand for alternate, sustainable and green energy sources.[2] In response to the higher demand for energy, researchers are attempting to explore new energy resources for sustainable and green energy to alleviate energy-related issues and avoid environmental contamination.[3,4] Renewable energy sources such as sun, wind, heat, *etc.* are good for the environment and alternatives to fossil fuels.[5]

Thermoelectric (TE) materials can change the heat/thermal energy of the sun or waste heat directly into electricity. These materials are suitable for making efficient thermoelectric devices for developing sustainable and green energy from waste heat.[6] Thermoelectric devices offer several benefits such as noiselessness, zero-emission, long service life,[7–9] no moving parts, accurate temperature control and the ability to function under challenging circumstances.[2] Now the efficiency of TE materials is figured out using a special formula: $ZT = S^2\sigma T/(\kappa_l + \kappa_e)$, where *ZT* is the figure of merit, *T* is the temperature, *S* depicts the Seebeck coefficient, σ represents the electrical conductivity, $S^2\sigma$ denotes the power factor (PF), κ_l is the lattice thermal conductivity, and κ_e is the electron thermal conductivity. The κ_l should be low and σ and *S* should be high for good thermoelectric materials.[10] In the ideal situation, reducing the κ_l would result in outstanding TE performance without decreasing the PF values of TE materials.

After the synthesis of Janus MoSSe[11] and Janus WSSe[12] monolayers, other Janus 2D compounds have been the subject of considerable investigation and attention toward thermal transport characteristics.[13] In crystal formations, their mirror asymmetry can reduce κ_l by increasing phonon anharmonicity.[14–16] For example, gallium chalcogenide-based Janus monolayers have been demonstrated with $\kappa_l \approx$ 11.95–26.16 W m^{-1} K^{-1},[14] significantly lower than those of conventional monolayers such as GaS ($\kappa_l \approx$ 100 W m^{-1} K^{-1}) and GaSe ($\kappa_l \approx$ 74 W m^{-1} K^{-1}) at 300 K.[15] The *ZT* value at 300 K of the Janus Al_2STe monolayer is reported to be 1.38 (n-type), comparatively greater than those for conventional Al-chalcogenide monolayers (*ZT* ≈ 0.52–0.59).[17] Furthermore, the Janus WSTe monolayer has a smaller κ_l than 2D WS_2, leading to a higher *ZT* at 1200 K of 2.56.[16]

Furthermore, several novel Janus monolayers like AsTeX (X = Cl, Br and I),[18] AsSBr,[19] NiSX (X = O, Se and Te),[20] In_2XO (X = S, Se and Te),[21] HfX_2 (X = S, Se),[22] PdSX (X = Se and Te),[23] BiOCl[24] and SbYZ (Y = S, Se; Z = Cl, Br and I)[25] with excellent thermoelectric properties (*ZT* ≈ 0.06–2.54 at ~300–900 K) have been reported. Hence, the Janus materials with excellent thermal and electron transport properties are suitable for advanced thermoelectric applications.

Advancing past their binary counterparts, 2D ternary metal chalcogenides[26] are becoming the next generation of 2D semiconductors.[27,28] In particular, ternary compounds based on

[a] *Department of Physics, Central University of Punjab, Bathinda-151401, India. E-mail: ashokphy@cup.edu.in*
[b] *Department of Physics, Dr Hari Singh Gour University, Sagar, M.P.-470003, India. E-mail: rgsolanki@dhsgsu.edu.in*

† Electronic supplementary information (ESI) available. See DOI: https://doi.org/10.1039/d4ma00924j

© 2025 The Author(s). Published by the Royal Society of Chemistry

Open Access Article. Published on 24 December 2024. Downloaded on 2/15/2026 7:07:25 PM.
This article is licensed under a Creative Commons Attribution-NonCommercial 3.0 Unported Licence.

bismuth, like bismuth oxychalcogenides (Bi_2O_2X where X = S, Se, and Te), have been recently realized, and their extraordinary qualities such as high carrier mobility and stability under ambient conditions have drawn a lot of attention.[29,30] Additionally, recent experimental research shows that bismuth oxyhalides (BiOX, where X = Cl, Br, and I) exhibit superior performance in energy harvesting applications because of their distinct electronic characteristics.[31] Also, in theoretical studies, BiOX (X = Cl, Br) has shown good thermochemical stability.[32] Another significant class of ternary frameworks composed of bismuth is Janus bismuth chalcogenides Bi_2X_2Y (X = Te, Se; Y = Te, Se, S), which have been shown to possess good energy harvesting potential.[33]

This work is inspired by the previous explorations of pnictogen-based dichalcogenide monolayers in a novel structure[34] for optoelectronic applications. We extensively studied the novel Janus monolayers BiYZ (Y ≠ Z = Te, Se and S) employing density functional theory (DFT). The dynamical stability and thermal stability of Janus BiYZ are confirmed by performing phonon dispersion and *ab initio* molecular dynamics (AIMD) simulations. We investigated the mechanical response for material stability. We examined that 2D BiYZ exhibits high thermoelectric performance having very low lattice thermal conductivity including electron–phonon interaction mechanisms. In accordance with the deformation potential theory, these monolayers exhibit high carrier mobility.

2. Computational details

The current study uses the quantum espresso (QE) software[35] to perform first-principles computations on Janus BiYZ monolayers using density functional theory (DFT). To compute the exchange–correlation energy, the GGA-PBE functional[36] was utilized. The valence electrons were described using potentials created by the projected-augmented-wave (PAW) approach.[37] The structures were optimized with gamma (Γ) centered 12 × 12 × 1 *k*-meshes. The electron convergence for energy and force was set at 10^{-8} eV and 10^{-7} eV Å^{-1} respectively, for structure relaxation within a plane-wave kinetic energy cutoff of 80 Ry. The *z*-direction was maintained at 20 Å vacuum to avoid interactions between neighboring images of supercell. Density functional perturbation theory (DFPT) computations were performed using dynamical matrices on 16 × 16 × 1 *k*-point mesh and 6 × 6 × 1 Γ-centered *q*-point grid to simulate the phonon dispersion spectra.[38] AIMD calculations using a Nosé–Hoover thermostat[39,40] were performed with a time step of 1 fs for 5000 fs. The thermoelectric transport coefficients such as electron thermal conductivity (κ_e) and electrical RTA (relaxation time approximation)[29] were determined using the BoltzTrap code[41] *via* semi-classical Boltzmann transport equations (BTE). According to RTA, electronic thermal conductivity (κ_e/τ) and (σ/τ) are estimated using BoltzTraP within the BTE framework. The EPW software,[42,43] which makes use of maximally localized Wannier functions (MLWFs) for effective interpolation of electron–phonon interaction (EPI) matrix components onto a fine *k*- and *q*-mesh[32,44–48] of 80 × 80 × 1, was used to calculate the relaxation time. Phono3py[49] which is interfaced with the QE package was adopted to calculate the lattice thermal conductivity (κ_l). A 3 × 3 × 1 supercell was used to obtain interatomic force constants of 2nd and 3rd order, with 4 × 4 × 1 *k*-point sampling.

3. Results and discussion

3.1 Geometrical structure and stability analysis

The optimized structures of Janus BiYZ monolayers with a *cm*11 space group (no. 13) are shown in Fig. 1. There are six atoms in the unit cell with a rhombus structure and 12 atoms in a rectangular unit cell. Table 1 lists the structural parameters of Janus monolayers. In this work, we adopted a rhombus unit cell for all the material properties except for the mechanical response where a rectangular unit cell is used. With an increase in the radius of constituent atoms, the lattice constant (*a* = *b*) of Janus BiYZ monolayers increases (Table 1). Moreover, the reduced attractive forces among the atoms with bigger radii lead to a rise in total thickness (*h*) and bond lengths (d_{Bi-Y}, and d_{Bi-Z}), while bond angles decreased with larger atoms of Janus BiYZ monolayers, as shown in Table 1. The Janus BiYZ monolayers' estimated structural properties fall between those of their parent monolayers. Our calculated values of parent monolayers BiY_2 (Y = S, Se, Te) are consistent with the prior literature.[34]

We computed the cohesive energies to determine the energetic stability of monolayers as:

$$E_{coh}\left(E_{BiY_2/BiYZ}\right) = \frac{E_{BiY_2/BiYZ} - mE_{Bi} - nE_Y \text{ or } (nE_Y - oE_Z)}{6} \quad (1)$$

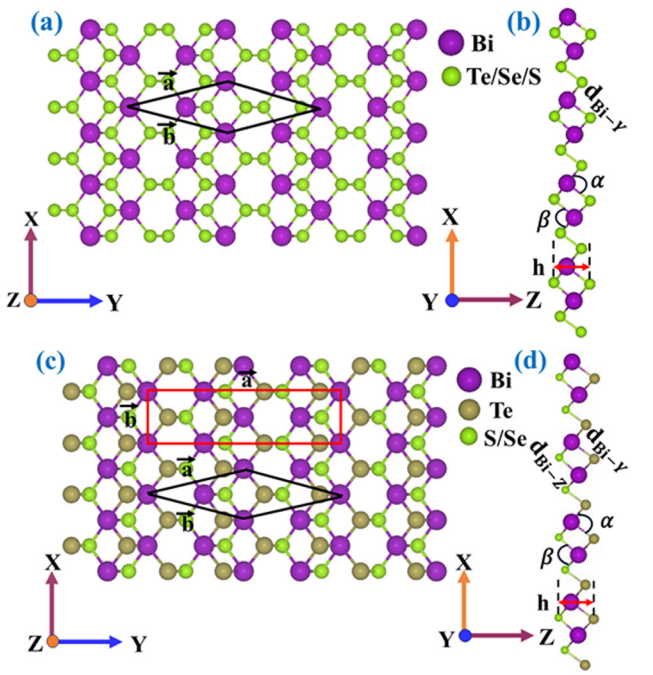

Fig. 1 The top (a) and side (b) views of BiY_2 (Y = Te, Se and S) monolayers and top (c) and side (d) views of Janus BiYZ (Y ≠ Z = Te, Se and S) monolayers. The rhombus (with black color) and rectangular (with red color) unit cells utilized in the computations are displayed. The related lattice vectors (*a* and *b*), bond angles (*α* and *β*), bond lengths (d_{Bi-Y}, and d_{Bi-Z}) and thickness (*h*) of the Janus BiYZ (Y ≠ Z = S, Se, Te) monolayers are also shown.

© 2025 The Author(s). Published by the Royal Society of Chemistry

Open Access Article. Published on 24 December 2024. Downloaded on 2/15/2026 7:07:25 PM. This article is licensed under a Creative Commons Attribution-NonCommercial 3.0 Unported Licence.

Table 1 The optimized lattice parameters (a and b), atomic bond lengths (d_{Bi-Y}, and d_{Bi-Z}), bond angles between Y–Bi–Y and Z–Bi–Z (α and β), thickness (h), work functions (Φ_Y, Φ_Z,) for different surfaces Y and Z, and their differences $\Delta\Phi$ and cohesive energy (E_{coh}) for Janus BiYZ (Y ≠ Z = S, Se, Te) and BiY_2 (Y = Te, Se, S) monolayers

2D monolayers	(a,b) (Å)	d_{Bi-Y}, d (Å)	d_{Bi-Z} d (Å)	α (°)	β (°)	h (Å)	Φ_W (eV)	Φ_X (eV)	$\Delta\Phi$ (eV)	E_{coh} (eV per atom)
$BiTe_2$	8.53	2.89	—	87.76	92.23	4.39	4.33	4.33	0	4.68
$BiSe_2$	7.86	2.70	—	89.85	90.14	4.01	4.85	4.85	0	4.55
BiS_2	7.59	2.57	—	92.25	87.74	3.75	5.06	5.06	0	4.34
BiTeSe	8.22	2.89	2.70	87.63	90.38	4.21	3.20	3.26	0.06	3.57
BiTeS	8.13	2.88	2.56	85.58	90.94	4.09	2.98	2.93	0.05	3.74
BiSeS	7.74	2.96	2.57	87.27	89.98	3.88	3.20	3.18	0.02	3.95

where E_{BiYZ} is the total energy of BiYZ, and E_{Bi}, E_Y, E_Y and E_Z are single atom energies of Bi, Y and Z elements, respectively. m, n and o represent the atom counts in the respective unit cells.

The cohesive energies of Janus BiTeSe, BiTeS, and BiSeS monolayers are in between the cohesive energies of their constituent parent monolayer counterparts (Table 1). The computed E_{coh} of Janus BiYZ monolayers is comparable to those of Janus SbXY (3.21–3.84 eV per atom),[25] BiXY (2.46–3.58 eV per atom)[44] and Ge_2XX' (3.14–3.68 eV per atom)[45] monolayers, indicating the energetic stability of Janus BiYZ monolayers and their possibility of experimental synthesis.

In addition, we compute the work function Φ, which is an important electron property. Fig. S1(a)–(e), ESI† demonstrates the average electrostatic potential energy curves of BiY_2 and Janus BiYZ along the thickness of the monolayers where the dipole correction is included. Table 1 shows the work function of two different surfaces Φ_X and Φ_Y along with their difference $\Delta\Phi$. As effective electron emission is desired in electronic and optoelectronic devices, the observed alterations in the work function may have important significance for future applications.[46]

3.1.1 Dynamical and thermal stability. We then investigate Janus BiYZ monolayers' dynamical and thermal stability. By computing phonon dispersion spectra, Janus BiYZ monolayers' dynamical stability is verified. The absence of imaginary frequencies in the phonon dispersion spectra of Janus BiYZ monolayers suggests that these monolayers are dynamically stable, as seen in Fig. 2(a)–(c). The dispersion spectra of BiYZ monolayers show eighteen vibrational modes, *i.e.*, three acoustic phonon (AP) modes (flexural acoustic (ZA) branch, the transverse acoustic (TA) branch, and the longitudinal acoustic (LA)) and 15 optical phonon (OP) modes. Similar to other 2D monolayers predicted by the continuum elasticity theory, the ZA branch displays quadratic dispersion while the TA and LA branches exhibit linear dispersion around the Γ-point. As the atomic mass of constituent atoms became larger, the phonon modes of BiYZ monolayers changed to lower frequencies as shown in Fig. 2(a)–(c). Because of the weak bond between the atoms in BiSeS, a gap appears between the AP and OP modes. Next, AIMD simulations are used to assess the thermal stability of the Janus BiTeSe, BiTeS, and BiSeS monolayers at room temperature (300 K) using a comparatively bigger 4 × 4 × 1 supercell. Fig. 2(d)–(f) depicts the small thermal fluctuation in temperature and energy as a function of the simulated time steps at room temperature. The significantly less distortion of monolayer structures without bond-breaking suggests that the Janus BiTeSe, BiTeS, and BiSeS monolayers are thermally stable.

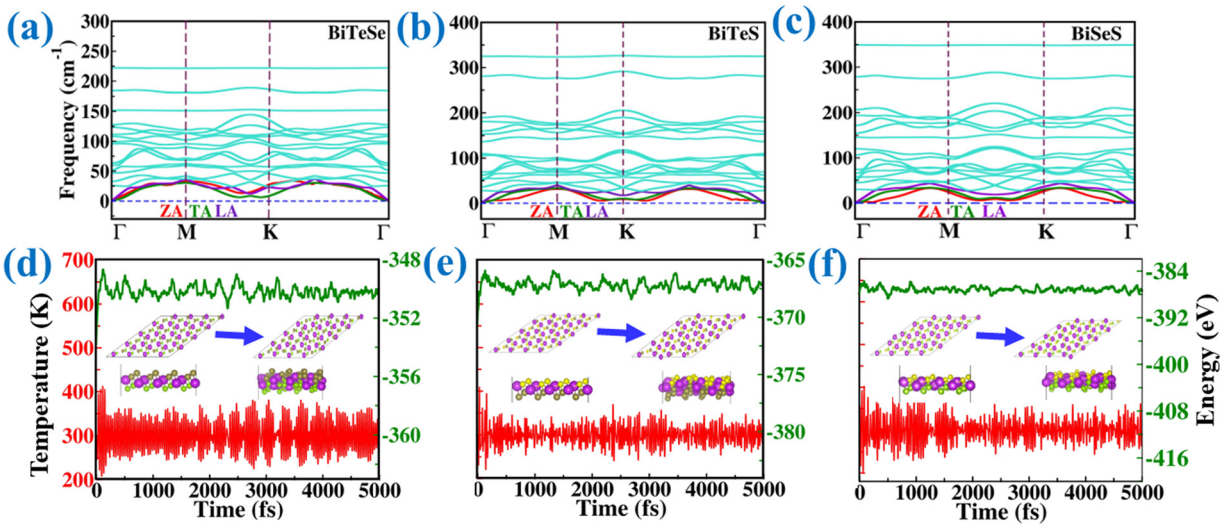

Fig. 2 (a)–(c) Phonon dispersion spectrum with flexural acoustical (ZA), transverse acoustical (TA) and longitudinal acoustical (LA) phonon modes and (d)–(f) the AIMD energy and temperature fluctuations at 300 K of Janus BiYZ (Y ≠ Z = S, Se, Te) monolayers. The snapshots of Janus monolayers after 5000 fs AIMD simulations are also shown.

Open Access Article. Published on 24 December 2024. Downloaded on 2/15/2026 7:07:25 PM. This article is licensed under a Creative Commons Attribution-NonCommercial 3.0 Unported Licence.

3.1.2 Mechanical stability. Following the unveiling of the structural stability, the mechanical stability of the suggested structures as determined by the Born and Huang criteria[47] is examined by computing the elastic strain tensor. The non-zero elastic constants C_{ij} such as C_{11}, C_{12}, and C_{66} are obtained as shown in Table 2. 2D Janus BiYZ monolayers' mechanical stability satisfies $C_{11} > |C_{12}|$ and C_{66} $(C_{11} - C_{12})/2 > 0$ indicating their mechanical stability.

The elastic characteristics of BiYZ monolayers are analyzed using two constants: the Young's modulus (Y_{2D}) and the Poisson ratio (ν):

$$Y_{2D} = \frac{(C_{11}{}^2 - C_{12}{}^2)}{C_{11}} \quad (2)$$

$$\nu = \frac{C_{12}}{C_{11}} \quad (3)$$

The computed values of Poisson's ratio (ν) for Janus BiTeSe, BiTeS and BiSeS monolayers are listed in Table 2. The value of Poisson's ratio for monolayers BiTeSe and BiSeS is the same as 0.32 which is less than one-third, implying that these monolayers are fragile according to the Frantsevich rule[48] whereas Janus BiTeS monolayers show a ductile nature. The Y_{2D} values of Janus BiYZ monolayers are listed in Table 2, which are higher than those of the Janus SbYZ (Y = S and Se and Z = Cl, Br, and I)[25] (0.28–0.38 N m^{-1}) and Ga_2SX_2 (X = O, S, Se, Te)[50] (20.8–116.08 N m^{-1}) monolayers and XBi_2Se_4 (X = Sn Pb)[51] (79.32 N m^{-1}) and comparable to that of the MoS_2 (130 N m^{-1})[52] monolayer.

3.2 Electronic structure

The band structures of Janus BiYZ monolayers are obtained using the PBE and PBE + SOC level of theory along high-symmetry paths of the Brillouin zone (Fig. 3(a)–(c)). The calculated band gaps with PBE (PBE + SOC) of Janus BiTeSe, BiTeS and BiSeS monolayers are 1.02 eV (0.50 eV), 1.07 eV (0.57 eV) and 1.44 eV (0.96 eV), respectively, which underscore the importance of including SOC effects in the studied monolayers. As an indirect bandgap semiconductor, the Janus monolayers are found to have the valence-band maximum (VBM) and conduction-band minimum (CBM) on the Γ point along the Γ–K direction. Considering SOC effects, the bandgap decreases in these monolayers due to heavy Bi and Te atoms. The band gaps of the corresponding parent $BiTe_2$, $BiSe_2$, and BiS_2 monolayers using PBE (PBE + SOC) are calculated to be 0.92 eV (0.32 eV), 1.29 eV (0.80 eV) and 1.59 eV (0.93 eV) as depicted in Fig. S2(a)–(c), ESI.† These values are consistent with previously reported bandgaps of these monolayers.[34] We also calculated the partial density of states (PDOS) to further analyze the electronic structure. The PDOS analysis (Fig. S3(a)–(c), ESI†) reveals that the p-orbitals are involved in the states near the Fermi energy of BiYZ monolayers.

Furthermore, we investigated the Janus BiYZ monolayer's optical characteristics in a broad range of 0–10 eV of photon energy $\hbar\omega$, with the incoming photon being parallel polarized. The optical absorbance that has been used to analyze is given as:

$$A(\omega) = \frac{\omega}{c} L\varepsilon_2(\omega) \quad (4)$$

where L denotes the cell's length in the Z-direction. Fig. S4, ESI† clearly shows in-plane light absorption maxima in the notably visible range (1.75–8 eV), suggesting potential uses of these materials in optoelectronic devices.

3.2.1 Carrier mobility. The materials' suitability for use in electronic devices is largely determined by their electronic transport characteristics, particularly carrier mobility (μ_{2D}). Deformation potential approximation (DPA) is a widely used technique for determining the carrier mobility,[53] μ_{2D} of 2D materials, which was first proposed by Bardeen and Shockley and can be written as:[53–55]

$$\mu_{2D} = \frac{e\hbar^3 C_{2D}}{k_B T m^* m_d E_d{}^2} \quad (5)$$

where $\hbar$ is the Planck constant, e is the electron charge, T is the temperature, which is fixed at 300 K, k_B is the Boltzmann constant, C_{2D} indicates elastic constants, m^* represents effective masses of electron and holes, $m_d = \sqrt{m_x^* m_y^*}$ is the average effective mass and E_d is the deformation potential (DP) constant. The DP constant is obtained by calculating the band edges and concerning the uniaxial strain (Fig. S5, ESI†). The effective mass and deformation potential of Janus BiYZ monolayers are comparable with those of TlAgX (X = S, Se) monolayers[56] and HG monolayers.[57] It is determined that the carrier mobility of Janus BiYZ monolayers is highly anisotropic, indicating directional dependence of the effective masses and deformation potentials of holes and electrons. The values of μ_{2D} of Janus BiYZ monolayers for both electrons and holes are listed in Table 3. Note that the electron (hole) mobility of the Janus $SMoSiN_2$ monolayer is 298.7 (1377.9) cm^2 V^{-1} s^{-1}.[58] Also the electronic mobility of layered $PbBi_2Se_4$ is estimated to be 153 cm^2 V^{-1} s^{-1}.[59] The Janus BiYZ monolayers also possess mobilities higher than those of other Janus monolayers such as MoSSe (250 cm^2 V^{-1} s^{-1} (ref. 60)), HG (14.18×10^3 cm^2 V^{-1} s^{-1}) and $Mo_8S_6Se_6$ (104 cm^2 V^{-1} s^{-1}),[61] suggesting that these Janus monolayers would be promising materials for electronic and thermoelectric applications.

Table 2 Elastic coefficients (C_{11}, C_{12}), Young's modulus (Y_{2D}) and Poisson's ratio (ν) of Janus BiYZ (Y ≠ Z = S, Se, Te) monolayers

2D monolayers	C_{11} (N m^{-1})	C_{12} (N m^{-1})	Y_{2D} (N m^{-1})	Poisson's ratio (ν)
BiTeSe	160.46	52.50	143.28	0.32
BiTeS	180.76	86.20	148.63	0.42
BiSeS	260.42	94.08	226.43	0.32

3.3 Thermoelectric properties

3.3.1 Lattice thermal transport properties. The lattice thermal conductivity (κ_l) calculation relies heavily on the phonon transport parameters. Gruneisen parameter (γ) and phonon group velocity (v_k) are phonon transport characteristics that characterise the κ_l of Janus BiYZ monolayers. By aggregating the contributions of all phonon modes represented by the wave vector q and the dispersion branch λ, one may evaluate the κ_l,

© 2025 The Author(s). Published by the Royal Society of Chemistry

Open Access Article. Published on 24 December 2024. Downloaded on 2/15/2026 7:07:25 PM.
This article is licensed under a Creative Commons Attribution-NonCommercial 3.0 Unported Licence.

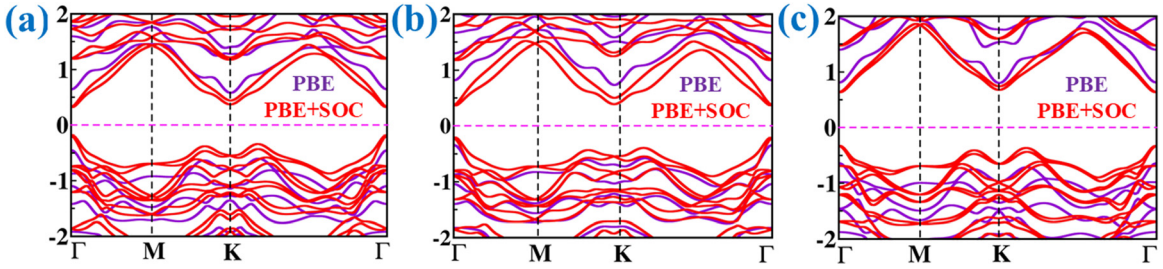

Fig. 3 The calculated band structure of Janus (a) BiTeSe, (b) BiTeS and (c) BiSeS monolayers with PBE (violet color) and PBE + SOC (red color) level of theory.

Table 3 The effective mass (m^*), average effective mass (m_d), deformation potential E_d (eV), elastic modulus C_{2D} (J m^{-2}) and charge carrier mobilities μ_{2D} (cm^2 V^{-1} s^{-1}) along the x- and y-directions of the Janus BiYZ (Y/Z = Te, Se, S) monolayers

Materials	Carrier	m_x^*	m_y^*	m_d	$C_{2D\text{-}X}$	$C_{2D\text{-}Y}$	$E_{d\text{-}X}$	$E_{d\text{-}Y}$	$\mu_{2D\text{-}X}$	$\mu_{2D\text{-}Y}$
BiTeSe	Electron	0.44	0.27	0.14	30.25	43.03	2.74	2.55	538	4000
	Hole	0.43	0.30	1.05			1.14	4.35	5903	1411
BiTeS	Electron	0.29	0.28	0.13	16.29	28.81	3.38	0.74	816	2353
	Hole	0.17	0.24	0.11			1.19	2.85	12 573	33 099
BiSeS	Electron	1.09	0.27	0.28	17.09	30.29	1.11	1.03	16 367	15 126
	Hole	0.53	0.20	0.56			0.27	0.53	4280	12 920

as the following equation:[62]

$$\kappa_l = \sum_{\lambda}^{3N} \int_q {v_{\lambda q}}^2 c_{\lambda q} \tau_{\lambda q} \mathrm{d}q \quad (6)$$

where $C_{\lambda q}$ is the mode-specific heat capacity, $\tau_{\lambda q}$ is the phonon relaxation time of phonon mode with λ and q and $V_{\lambda q}$ is the group velocity of phonon mode.

Phonon–phonon anharmonic interactions affect the κ_l expected for 2D materials because of the Umklapp process and it decreases with temperature as $\kappa_l \propto 1/T$ (ref. 63) as shown in Fig. 4. The calculated values of κ_l at room temperature are 0.02 W m^{-1} K^{-1}, 0.20 W m^{-1} K^{-1} and 0.04 W m^{-1} K^{-1} for Janus BiTeSe, BiTeS and BiSeS monolayers, respectively, indicating good thermoelectric performance of these materials. The Janus BiYZ monolayers show ultralow values of κ_l similar to those of the well-known 2D Janus WSTe ($\kappa_l \approx$ 0.08 W m^{-1} K^{-1})[16] and TlPo monolayers ($\kappa_l \sim$ 0.17 W m^{-1} K^{-1}).[64]

Next, we obtain Debye temperature (Θ_D) which can be computed as:[65]

$$\frac{1}{{\Theta_D}^3} = \frac{1}{3}\left(\frac{1}{{\Theta_{LA}}^3} + \frac{1}{{\Theta_{TA}}^3} + \frac{1}{{\Theta_{ZA}}^3}\right) \quad (7)$$

where Θ_i is defined as $\Theta = \hbar\nu_m/k_B$ for each mode, i = ZA, TA, and LA. k_B, $\hbar$ and ν_m represent the Boltzmann constant, the Planck constant and the maximum frequency of normal mode vibration (Fig. S6(a)–(c), ESI†).

The Debye temperatures (Θ_D) of Janus BiYZ (Y ≠ Z = Te, Se, S) monolayers are comparable to those of other monolayers as listed in Table 4. Low Θ_D signifies that phonon modes are activated at low temperatures, which makes phonon scattering channels available at low temperatures. Consequently, the lattice thermal conductivity shows a decrease in the values.[66]

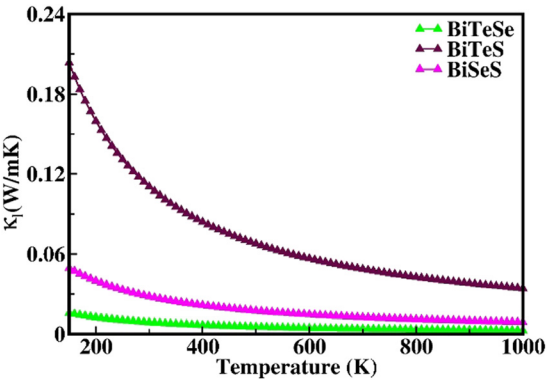

Fig. 4 Lattice thermal conductivity as a function of temperature for Janus BiYZ (Y ≠ Z = Te, Se, S) monolayers.

Also, the specific heat capacity (C_V) of Janus BiYZ (Y ≠ Z = Te, Se, S) monolayers is obtained in Fig. 5. The C_V of the Janus BiSeS monolayer (10.98 J mol^{-1} K^{-1}) is higher than that of the other two Janus BiTeSe (9.53 J mol^{-1} K^{-1}) and BiTeS (and 8.27 10.98 J mol^{-1} K^{-1}) monolayers. The C_V exhibits the anticipated T^3 law behaviour in the low-temperature limit.[72] After saturation, the C_V curve of these Janus monolayers remains constant with temperature. This type of behavior of the C_V curve is similar to that of other monolayers such as WXY (X, Y = S, Se, and Te),[73] PdXY (Y = Se, Te)[74] and M_2XY (M = Ga; X, Y = S, Se, Te).[14]

The most significant parameter for evaluating thermal transportation is the phonon group velocities which are expressed as:

$$v_k = \frac{\partial\omega_k(q)}{\partial q} \quad (8)$$

Open Access Article. Published on 24 December 2024. Downloaded on 2/15/2026 7:07:25 PM. This article is licensed under a Creative Commons Attribution-NonCommercial 3.0 Unported Licence.

Table 4 The Debye temperature (Θ_D) for Janus BiYZ (Y ≠ Z = Te, Se, S) monolayers

Materials	(Θ_D) (K)	
BiTeSe	74.22	This work
BiTeS	77.39	This work
BiSeS	79.95	This work
PdSeTe	60	67
SbTeI	86.4	68
BiTeI	82.1	
PbI_2	69	69
$PdSe_2$	63	70
$PdTe_2$	45	
SnSe	52	71

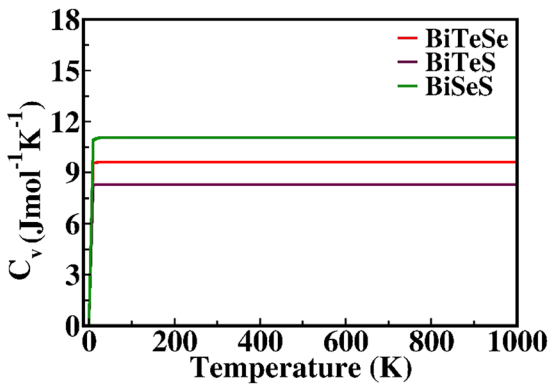

Fig. 5 Temperature dependence of specific heat capacity (C_V) of Janus BiYZ (Y ≠ Z = Te, Se, S) monolayers.

where k, ω and q represent the frequency of wave vector, phonon modes and vibrational mode index, respectively. In monolayer systems, the acoustic modes typically dominate the κ_l.[75] The high-frequency modes show relatively small group velocities, while the low-frequency zone displays larger values of group velocities. The calculated low group velocities 6.2, 4.9, and 3.6 km s^{-1} of BiTeSe, BiTeS and BiSeS from ZA mode (Fig. S6(a)–(c), ESI†) is the reason for the ultralow lattice thermal conductivity. Also, as seen in Fig. S7 (ESI†), Janus BiYZ monolayer's phonon lifetime mostly lies between 0.1 and 2.9 ps. The κ_l is also decreased by the small phonon relaxation time.

To further get deeper insight into the low lattice thermal conductivity, for every phonon mode, the Grüneisen parameter is computed to measure the anharmonicity of monolayers. The Grüneisen parameter (γ) is evaluated as:[76]

$$\gamma_k(q) = -\frac{a_0}{\omega_k(q)}\frac{\partial\omega_k(q)}{\partial a} \quad (9)$$

where a_0 is the equilibrium lattice constant. From eqn (8), we notice that a larger Grüneisen parameter is observable in the low-frequency domain as shown in Fig. S6(d)–(f), ESI.† Usually, a larger Grüneisen parameter indicates strong anharmonicity, which is also responsible for the ultralow value of κ_l.

3.3.2 Electronic transport properties. The carriers' semi-classical Boltzmann transport equations (BTE) are solved to derive the thermoelectric transport properties under relaxation time approximation (RTA) theories. Proper handling of the carrier relaxation time through intricate scattering processes is crucial in this case. Previous works have employed the deformation potential theory, in which the computed value is typically exaggerated and the relaxation time is represented as a constant.[77] In the current study, we use complete electron–phonon interactions to obtain the relaxation time from the imaginary component of the electron self-energy. The k-resolved relaxation time can be estimated as:

$$\sum_{nk}^{EP} = \sum_{qv,m} \omega_q \left|g^v_{mn}(k,q)\right|^2 \times \left[\frac{n_{qv}+f_{mk+q}}{\varepsilon_{nk}-\varepsilon_{mk+q}+\hbar\omega_{qv}-i\delta}+\frac{n_{qv}+1-f_{mk+q}}{\varepsilon_{nk}-\varepsilon_{mk+q}-\hbar\omega_{qv}-i\delta}\right] \quad (10)$$

where ω_q is the BZ weight associated with wave vector q of phonons, $g^v_{mn} = \left(\frac{\hbar}{2m_0\omega_{qv}}\right)^{\frac{1}{2}}\langle\Psi_{mk+q}|\partial_{qv}V|\Psi_{nk}\rangle$ is the electron–phonon coupling strength, and Ψ_{nk} represents the electronic wave function for eigenvalue ε_{nk}, wave-vector k and band index m. ω_{qv} is derivative of the self-consistent potential $\partial_{qv}V$ with branch index v and wave vector $q\cdot f_{mk+q}$ represent the electronic state occupation. The relaxation time as a function of carrier's energy is shown in Fig. 6(a)–(c). The estimated value of relaxation time is of the order of $\sim 10^{-15}$ s at different temperatures for Janus BiYZ monolayers.

The Wiedemann–Franz law[78] states that the electronic thermal conductivity κ_e can be calculated as follows:

$$\kappa_e = L\sigma T \quad (11)$$

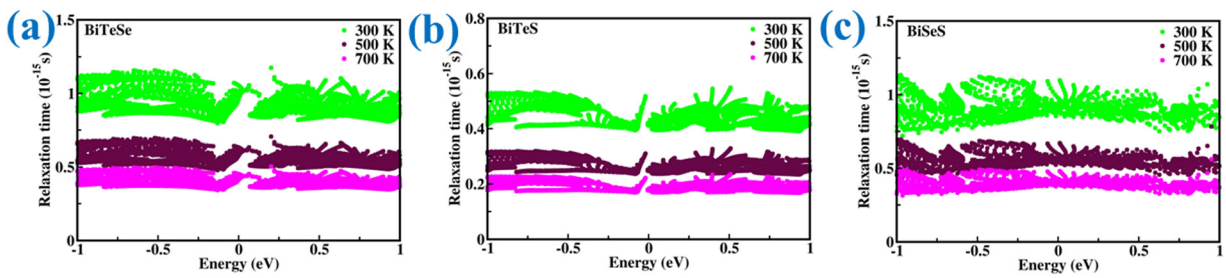

Fig. 6 The relaxation time as a function of carrier's energy of Janus BiYZ (Y ≠ Z = Te, Se, S) monolayers. Zero represents the Fermi energy.

© 2025 The Author(s). Published by the Royal Society of Chemistry

Open Access Article. Published on 24 December 2024. Downloaded on 2/15/2026 7:07:25 PM. This article is licensed under a Creative Commons Attribution-NonCommercial 3.0 Unported Licence.

where L represents the Lorenz constant; based on the Seebeck coefficient (S), we can calculate the Lorenz numbers using the formula $L = 1.5 + \exp\left[-\left|\frac{S}{116}\right|\right]$;[78] T is the temperature and σ is the electrical conductivity. The κ_e with variation of chemical potential ranges from ~0.4 to ~1.5 W m^{-1} K^{-1} at 500 K of Janus BiYZ monolayers (Fig. 7(a)). The variations of κ_e with chemical potential at temperatures 300 K and 700 K are also shown in Fig. S8(a), ESI.†

Moreover, the electrical conductivity and Seebeck coefficient of BiYZ monolayers are computed within the context of Boltzmann transport theory utilizing the equations:

$$S = -\frac{1}{eT}\frac{\sum_{n,k}(E_{nk} - E_F)v_{nk}{}^2\tau_{nk}\frac{\partial f_{nk}}{E}}{\sum_{n,k}v_{nk}{}^2\tau_{nk}\frac{\partial f_{nk}}{E}}, \quad (12)$$

$$\frac{\sigma}{\tau_{nk}} = -\frac{2e^2}{NV}\sum_{n,k}v_{nk}{}^2\tau_{nk}\frac{\partial f_{nk}}{\delta E}, \quad (13)$$

where T is the electronic temperature, V is the cell volume, f_{nk} is the Fermi–Dirac distribution function, E_F is the Fermi energy, V_{nk} is an aspect of group velocity in a specific direction at each k point and N depicts the k point number.

In addition, the electrical conductivity, Seebeck coefficient, and power factor ($P = S^2\sigma$) concerning chemical potential at 500 K are presented in Fig. 7(b)–(d) and also in Fig. S8(b)–(d) (ESI†) at 300 K and 700 K. The increase in temperature decreases the value of S. The highest values of power factor obtained at 500 K temperature for p(n)-type carriers are 0.14×10^{-3} W m^{-1} K^{-2} (0.05×10^{-3} W m^{-1} K^{-2}), 0.02×10^{-3} W m^{-1} K^{-2} (0.03×10^{-3} W m^{-1} K^{-2}), and 0.08×10^{-3} W m^{-1} K^{-2} (0.05×10^{-3} W m^{-1} K^{-2}) of Janus BiTeSe, BiTeS and BiSeS monolayers, respectively. The maximum value of power factor indicates that BiTeSe and BiSSe are p-type while BiTeS is an n-type semiconductor due to the high Seebeck coefficient as displayed in Fig. 7(c) at 500 K and Fig. S8(c), ESI† at 300–700 K. The power factor of these monolayers is comparable to that of the Janus 2D B_2P_6 monolayer.[79]

3.3.3 Thermoelectric figure of merit. A high thermoelectric figure-of-merit (ZT) value requires large values of σ and S and considerably small values of κ_e and κ_l as shown by the expression:

$$ZT = S^2\sigma T/(\kappa_l + \kappa_e) \quad (14)$$

The assumption of constant relaxation time does not consider electron–phonon interactions. We computed accurate relaxation time by considering electron–phonon interactions using the EPI method. Fig. 8(a)–(c) demonstrates the figure-of-merit (ZT) for a p-(n)-type of Janus BiYZ monolayers with respect to chemical potential. The maximum ZT values of Janus BiTeSe, BiTeS, and BiSeS monolayers obtained at 500 K are 0.97 (0.76), 0.46 (0.60), and 1.78 (1.35) for p-(n)-type carriers. Table S1, ESI† shows that ZT values for monolayers BiTeSe, BiTeS, and BiSeS are high enough at 700 K. Table 5 displays the thermoelectric performance of previously reported thermoelectric materials comparable with BiYZ monolayers. A weighted average of the thermoelectric figure-of-merit ($z\bar{T}$) is used to obtain the thermoelectric efficiency η_{max} (%) as:[80,81]

$$\eta_{max} = \frac{T_H - T_C}{T_H}\frac{\sqrt{1 + z\bar{T}} - 1}{\sqrt{1 + z\bar{T}} + \frac{T_C}{T_H}} \quad (15)$$

where T_c and T_H represent the cold and hot temperatures. Our calculations revealed that the thermoelectric unit's output

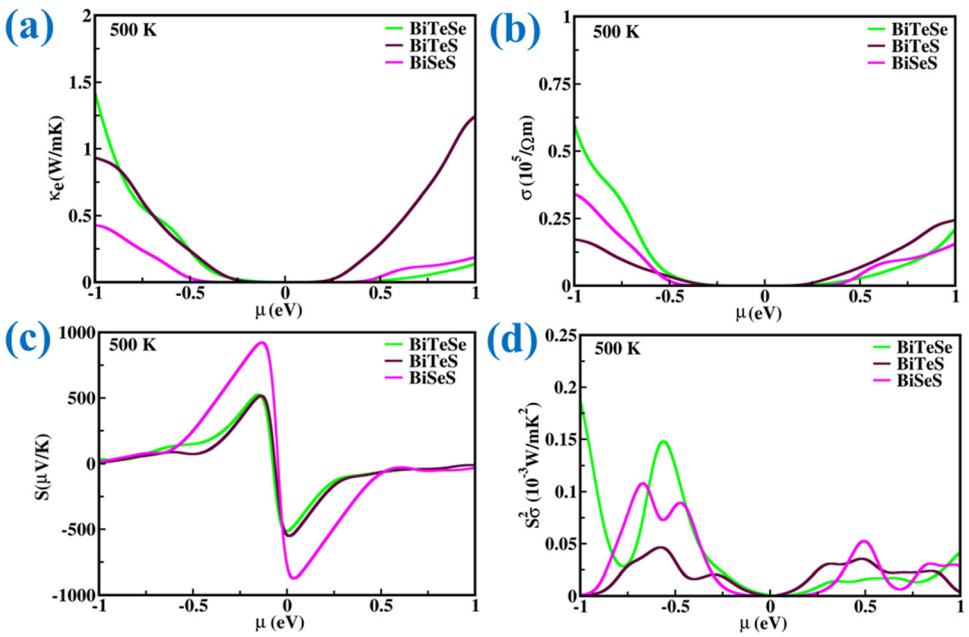

Fig. 7 The calculated (a) electronic thermal conductivity (κ_e), (b) electrical conductivity (σ), (c) Seebeck coefficient (S) and (d) power factor ($S^2\sigma$) of Janus BiYZ (Y ≠ Z = Te, Se, S) monolayers at 500 K.

Open Access Article. Published on 24 December 2024. Downloaded on 2/15/2026 7:07:25 PM.
This article is licensed under a Creative Commons Attribution-NonCommercial 3.0 Unported Licence.

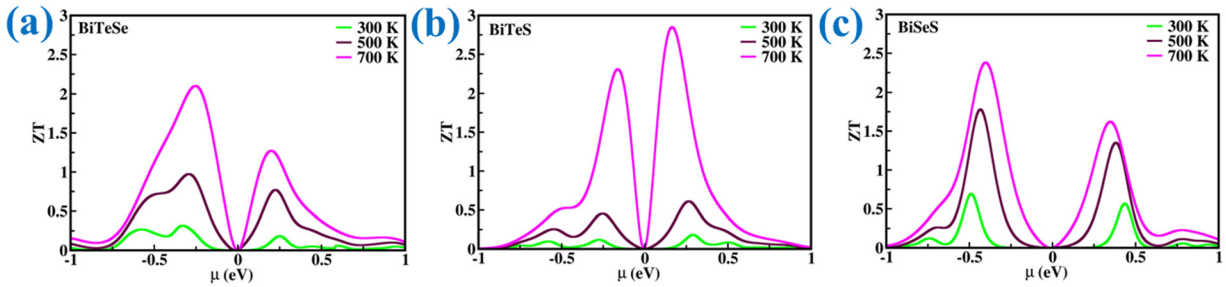

Fig. 8 The calculated figure-of-merit (*ZT*) concerning the chemical potential (μ) of Janus BiYZ (Y ≠ Z = Te, Se, S) monolayers at 300–700 K.

Table 5 The comparison of *ZT* of 2D Janus BiYZ monolayers with other similar monolayers at temperature 300–700 K

2D monolayers	Figure-of-merit (*ZT*)	Temperature (K)	Ref.
BiTeSe	0.18–2.11	300–700	This work
BiTeS	0.10–2.85	300–700	This work
BiSeS	0.58–2.38	300–700	This work
Janus BiSbTeSeS, BiSbTeSeTe, and BiSbTeSTe	035, 0.55, 0.70	300	84
Bi_2TeSe_2	0.87–3.45	300–900	13
Bi_2Te_2Se	1.4–2.0 (p)	300–500	85
Bi_2SSe_2	0.50–0.28 (p)	300–700	86
Bi_2S_2Se	1.39–0.93 (p)		
WSTe	0.742	300	16
TlPo	1.88	300	64
NiSO and NiSSe	~1	300	20
$ScYCBr_2$	~0.28–0.70	300–700	87
BaAgBi	0.42	300–600	88
γ-GeSe	0.84–2.04	300–600	89

power and efficiency could be increased up to 63.14% (57.90%), 53.76% (78.67%) and 64.14% (63.53%) of Janus BiTeSe, BiTeS and BiSeS monolayers for p-(n) type charge carriers, respectively. The reported TE efficiency of other 2D monolayers such as Bi_2Te_3[82] and X_2YH_2 (X = Si, Ge; Y = P, As, Sb, Bi)[83] is 5–18%. Also the TE efficiencies of Janus BiSbTeSeS, BiSbTeSeTe, and BiSbTeSTe monolayers are 34%, 30%, and 33%,[84] respectively. On comparison of the TE efficiency with other Janus monolayers, the reported efficiency is comparatively higher; hence, the Janus BiTeSe, BiTeS, and BiSeS monolayers are candidate materials for thermoelectric devices to convert waste heat directly into electricity.

Conclusions

In summary, the work reports a combined density functional theory and semi-classical Boltzmann transport calculations of Janus BiYZ (Y ≠ Z = Te, Se, S) monolayers. The dynamical stability for Janus BiYZ monolayers was verified from the phonon dispersion relations, which are free from imaginary frequencies. The elastic tensors and AIMD simulation represented that these Janus monolayers are thermally and mechanically stable. Poisson ratio (ν) and Young's modulus (Y_{2D}) are computed to investigate the mechanical response of suggested monolayers. The obtained band gaps of monolayers are indirect in nature with superior carrier mobility. The thermoelectric efficiency of these monolayers is calculated in the range of ~53–78%. The ultralow lattice thermal conductivity and high thermoelectric figure-of-merit make Janus BiYZ monolayers a promising candidate for thermoelectric devices.

Data availability

The data supporting this article have been included in this article and in the ESI.†

Conflicts of interest

The authors declared no conflicts of interest.

Acknowledgements

KM Sujata is thankful to the M.P. Council of Science and Technology MPCST (FTYS) for financial assistance in the form of a Young Scientist Fellowship. NV acknowledges the senior research fellowship from CSIR. The findings reported in this work were obtained using the computational facility at the Central University of Punjab, Bathinda.

References

1 G. Zhang and Y.-W. Zhang, Strain effects on thermoelectric properties of two-dimensional materials, *Mech. Mater.*, 2015, **91**, 382–398.

© 2025 The Author(s). Published by the Royal Society of Chemistry

Open Access Article. Published on 24 December 2024. Downloaded on 2/15/2026 7:07:25 PM. This article is licensed under a Creative Commons Attribution-NonCommercial 3.0 Unported Licence.

2 M. Hong and Z.-G. Chen, Chemistry in advancing thermoelectric GeTe materials, *Acc. Chem. Res.*, 2022, **55**(21), 3178–3190.
3 Z.-G. Chen, *et al.*, Nanostructured thermoelectric materials: Current research and future challenge, *Prog. Nat. Sci.:Mater. Int.*, 2012, **22**(6), 535–549.
4 T. Zhu, *et al.*, Compromise and synergy in high-efficiency thermoelectric materials, *Adv. Mater.*, 2017, **29**(14), 1605884.
5 A. R. Natarajan, *et al.*, Bulk and monolayer thermoelectric and optical properties of anisotropic NbS_2Cl_2, *Mater. Today Commun.*, 2023, **34**, 105309.
6 B. Ali, *et al.*, Optical and thermoelectric properties of new Janus $ZnMN_2$ (M = Ge, Sn, Si and N = S, Se, Te) monolayers: a first-principles study, *Nanoscale Adv.*, 2024, **6**(2), 680–689.
7 S. Ortega, *et al.*, Bottom-up engineering of thermoelectric nanomaterials and devices from solution-processed nanoparticle building blocks, *Chem. Soc. Rev.*, 2017, **46**(12), 3510–3528.
8 R. Kroon, *et al.*, Thermoelectric plastics: from design to synthesis, processing and structure–property relationships, *Chem. Soc. Rev.*, 2016, **45**(22), 6147–6164.
9 Z.-H. Ge, *et al.*, Low-cost, abundant binary sulfides as promising thermoelectric materials, *Mater. Today*, 2016, **19**(4), 227–239.
10 X.-L. Zhu, *et al.*, KAgX (X = S, Se): high-performance layered thermoelectric materials for medium-temperature applications, *ACS Appl. Mater. Interfaces*, 2020, **12**(32), 36102–36109.
11 J. Zhang, *et al.*, Janus monolayer transition-metal dichalcogenides, *ACS Nano*, 2017, **11**(8), 8192–8198.
12 B. Zheng, *et al.*, Band alignment engineering in two-dimensional lateral heterostructures, *J. Am. Chem. Soc.*, 2018, **140**(36), 11193–11197.
13 N. Wang, *et al.*, High-temperature thermoelectric monolayer Bi_2TeSe_2 with high power factor and ultralow thermal conductivity, *ACS Appl. Energy Mater.*, 2022, **5**(2), 2564–2572.
14 Q. Zhong, *et al.*, Phonon thermal transport in Janus single layer M2XY (M = Ga; X, Y = S, Se, Te): A study based on first-principles, *Phys. E*, 2020, **115**, 113683.
15 T. Pandey, D. S. Parker and L. Lindsay, *Ab initio* phonon thermal transport in monolayer InSe, GaSe, GaS, and alloys, *Nanotechnology*, 2017, **28**(45), 455706.
16 A. Patel, *et al.*, High thermoelectric performance in two-dimensional Janus monolayer material WS-X (X = Se and Te), *ACS Appl. Mater. Interfaces*, 2020, **12**(41), 46212–46219.
17 G. S. Khosa, *et al.*, Janus Al_2STe monolayer: a prospective thermoelectric material, *Solid State Commun.*, 2022, **341**, 114579.
18 P. Chauhan, J. Singh and A. Kumar, As-based ternary Janus monolayers for efficient thermoelectric and photocatalytic applications, *J. Mater. Chem. A*, 2023, **11**(19), 10413–10424.
19 M. Liu, *et al.*, Thermoelectric properties of Janus AsSBr monolayer from first-principles study, *Solid State Commun.*, 2022, **342**, 114612.
20 S. Ahmadi, *et al.*, A theoretical prediction of novel Janus NiSX (X = O, Se, Te) Monolayers: Electronic, optical, and thermoelectric properties, *Appl. Surf. Sci.*, 2023, **616**, 156560.
21 T. V. Vu, *et al.*, Theoretical prediction of electronic, transport, optical, and thermoelectric properties of Janus monolayers In_2XO (X = S, Se, Te), *Phys. Rev. B*, 2021, **103**(8), 085422.
22 J. Bera, A. Betal and S. Sahu, Spin orbit coupling induced enhancement of thermoelectric performance of HfX_2 (X = S, Se) and its Janus monolayer, *J. Alloys Compd.*, 2021, **872**, 159704.
23 W.-L. Tao, *et al.*, Thermoelectric properties of Janus MXY (M = Pd, Pt; X, Y = S, Se, Te) transition-metal dichalcogenide monolayers from first principles, *J. Appl. Phys.*, 2020, **127**(3), 035101.
24 C.-W. Wu, *et al.*, Enhanced high-temperature thermoelectric performance by strain engineering in BiOCl, *Phys. Rev. Appl.*, 2022, **18**(1), 014053.
25 P. Chauhan, J. Singh and A. Kumar, Two-dimensional Janus antimony chalcohalides for efficient energy conversion applications, *J. Mater. Chem. A*, 2024, **12**, 16129–16142.
26 L. Dong, J. Lou and V. B. Shenoy, Large in-plane and vertical piezoelectricity in Janus transition metal dichalchogenides, *ACS Nano*, 2017, **11**(8), 8242–8248.
27 A. Ramasubramaniam, Large excitonic effects in monolayers of molybdenum and tungsten dichalcogenides, *Phys. Rev. B: Condens. Matter Mater. Phys.*, 2012, **86**(11), 115409.
28 Q. Ji, *et al.*, Chemical vapour deposition of group-VIB metal dichalcogenide monolayers: engineered substrates from amorphous to single crystalline, *Chem. Soc. Rev.*, 2015, **44**(9), 2587–2602.
29 M. J. Varjovi and E. Durgun, First-principles study on structural, vibrational, elastic, piezoelectric, and electronic properties of the Janus Bi XY (X = S, Se, Te and Y = F, Cl, Br, I) monolayers, *Phys. Rev. Mater.*, 2021, **5**(10), 104001.
30 J. Wu, *et al.*, Controlled synthesis of high-mobility atomically thin bismuth oxyselenide crystals, *Nano Lett.*, 2017, **17**(5), 3021–3026.
31 J. Di, *et al.*, Bismuth oxyhalide layered materials for energy and environmental applications, *Nano Energy*, 2017, **41**, 172–192.
32 T. Das and S. Datta, Thermochemical stability, and electronic and dielectric properties of Janus bismuth oxyhalide BiOX (X = Cl, Br, I) monolayers, *Nanoscale Adv.*, 2020, **2**(3), 1090–1104.
33 S.-H. Cao, *et al.*, The coexistence of high piezoelectricity and superior optical absorption in Janus Bi_2X_2Y (X = Te, Se; Y = Te, Se, S) monolayers, *Phys. Chem. Chem. Phys.*, 2024, **26**(5), 4629–4642.
34 J. D. Mella, *et al.*, Prediction of BiS_2-type pnictogen dichalcogenide monolayers for optoelectronics, *npj 2D Mater. Appl.*, 2024, **8**(1), 4.
35 P. Giannozzi, *et al.*, Advanced capabilities for materials modelling with Quantum ESPRESSO, *J. Phys.: Condens. Matter*, 2017, **29**(46), 465901.
36 J. P. Perdew, K. Burke and M. Ernzerhof, Generalized gradient approximation made simple, *Phys. Rev. Lett.*, 1996, **77**(18), 3865.
37 G. Kresse and D. Joubert, From ultrasoft pseudopotentials to the projector augmented-wave method, *Phys. Rev. B: Condens. Matter Mater. Phys.*, 1999, **59**(3), 1758.
38 P. Giannozzi, *et al.*, *Ab initio* calculation of phonon dispersions in semiconductors, *Phys. Rev. B: Condens. Matter Mater. Phys.*, 1991, **43**(9), 7231.

Open Access Article. Published on 24 December 2024. Downloaded on 2/15/2026 7:07:25 PM. This article is licensed under a Creative Commons Attribution-NonCommercial 3.0 Unported Licence.

39 W. G. Hoover, Canonical dynamics: Equilibrium phase-space distributions, *Phys. Rev. A:At., Mol., Opt. Phys.*, 1985, **31**(3), 1695.
40 S. Nosé, An extension of the canonical ensemble molecular dynamics method, *Mol. Phys.*, 1986, **57**(1), 187–191.
41 W. X. Zhou, *et al.*, Thermal conductivity of amorphous materials, *Adv. Funct. Mater.*, 2020, **30**(8), 1903829.
42 J. Noffsinger, *et al.*, EPW: A program for calculating the electron–phonon coupling using maximally localized Wannier functions, *Comput. Phys. Commun.*, 2010, **181**(12), 2140–2148.
43 H. Lee, *et al.*, Electron–phonon physics from first principles using the EPW code, *npj Comput. Mater.*, 2023, **9**(1), 156.
44 M. J. Varjovi and E. Durgun, First-principles study on structural, vibrational, elastic, piezoelectric, and electronic properties of the Janus BiXY (X = S, Se, Te and Y = F, Cl, Br, I) monolayers, *Phys. Rev. Mater.*, 2021, **5**(10), 104001.
45 M. J. Varjovi, S. Ershadrad and B. Sanyal, Structural, vibrational, elastic, electronic, and piezoelectric properties of binary γ-GeX and ternary γ-Ge_2XX' monolayers (X, X′ = S, Se, and Te), *Phys. Rev. B*, 2023, **107**(19), 195421.
46 N. Al Bouzieh, M. Benkraouda and N. Amrane, Exploring Hafnium-induced transformations in SnSe allotropes: Insights into structural, electronic, optical, and mechanical modifications for enhanced optoelectronic utilization, *Mater. Today Commun.*, 2024, **38**, 107574.
47 F. Mouhat and F.-X. Coudert, Necessary and sufficient elastic stability conditions in various crystal systems, *Phys. Rev. B: Condens. Matter Mater. Phys.*, 2014, **90**(22), 224104.
48 I. N. Frantsevich, *Elastic constants and elastic moduli of metals and insulators*, *Reference book*, 1982.
49 A. Togo, L. Chaput and I. Tanaka, Distributions of phonon lifetimes in Brillouin zones, *Phys. Rev. B: Condens. Matter Mater. Phys.*, 2015, **91**(9), 094306.
50 N. N. Hieu, *et al.*, Structural, electronic, and transport properties of quintuple atomic Janus monolayers Ga_2SX_2 (X = O, S, Se, Te): First-principles predictions, *Phys. Rev. B*, 2022, **105**(7), 075402.
51 C. Yao, *et al.*, Single-layer XBi_2Se_4 (X = Sn Pb) with multi-valley band structures and excellent thermoelectric performance, *Ceram. Int.*, 2023, **49**(15), 25455–25462.
52 R. C. Cooper, *et al.*, Nonlinear elastic behavior of two-dimensional molybdenum disulfide, *Phys. Rev. B: Condens. Matter Mater. Phys.*, 2013, **87**(3), 035423.
53 J. Bardeen and W. Shockley, Deformation potentials and mobilities in non-polar crystals, *Phys. Rev.*, 1950, **80**(1), 72.
54 P. L. Tran, *et al.*, First-principles examination of two-dimensional Janus quintuple-layer atomic structures $XCrSiN_2$ (X = S, Se, and Te), *Nanoscale Adv.*, 2023, **5**(11), 3104–3113.
55 Y. Liu, *et al.*, Monolayer $Bi_2Se_{3-x}Te_x$: novel two-dimensional semiconductors with excellent stability and high electron mobility, *Phys. Chem. Chem. Phys.*, 2020, **22**(17), 9685–9692.
56 Q. Zhang, *et al.*, Tl-based TlAgX (X = S, Se) monolayers with ultra-low lattice thermal conductivity and high ZT: a first-principles study, *J. Mater. Sci.*, 2022, **57**(47), 21607–21619.
57 D. Singh, V. Shukla and R. Ahuja, Optical excitations and thermoelectric properties of two-dimensional holey graphene, *Phys. Rev. B*, 2020, **102**(7), 075444.
58 S. G. Rudi, *et al.*, Enhanced performance of Janus $XMSiY_2$ (X = S, Se; M = Mo, W; and Y = N, P) monolayers for photocatalytic water splitting via strain engineering, *J. Phys. Chem. Solids*, 2023, **181**, 111561.
59 A. Chatterjee, S. N. Guin and K. Biswas, Ultrathin septuple layered $PbBi_2Se_4$ nanosheets, *Phys. Chem. Chem. Phys.*, 2014, **16**(28), 14635–14639.
60 W.-J. Yin, *et al.*, The unique carrier mobility of monolayer Janus MoSSe nanoribbons: a first-principles study, *Dalton Trans.*, 2021, **50**(29), 10252–10260.
61 Y. Peng, *et al.*, Prediction of high carrier mobility for novel Janus Mo8S6Se6 monolayers with different phases: first principles calculations, *J. Mater. Chem. C*, 2024, **12**, 15024–15031.
62 N. de Koker, Thermal conductivity of MgO periclase from equilibrium first principles molecular dynamics, *Phys. Rev. Lett.*, 2009, **103**(12), 125902.
63 X.-L. Zhu, *et al.*, High thermoelectric performance of new two-dimensional IV–VI compounds: A first-principles study, *J. Phys. Chem. C*, 2019, **124**(3), 1812–1819.
64 M. N. Çınar, *et al.*, Ballistic thermoelectric transport properties of two-dimensional group III–VI monolayers, *Phys. Rev. B*, 2021, **103**(16), 165422.
65 M. K. Mohanta, *et al.*, Ultra-low thermal conductivity and super-slow hot-carrier thermalization induced by a huge phononic gap in multifunctional nanoscale boron pnictides, *Phys. E*, 2020, **124**, 114222.
66 M. K. Mohanta, F. Is and A. De Sarkar, Valley Hall effect in graphene-like Sn X (X = Si, Ge) buckled monolayers with high charge carrier mobility and low lattice thermal conductivity, *Phys. Rev. B*, 2023, **107**(3), 035429.
67 H. Huang, *et al.*, Janus penta-PdSeTe: A two-dimensional candidate with high thermoelectric performance, *J. Alloys Compd.*, 2022, **924**, 166581.
68 S.-D. Guo, A.-X. Zhang and H.-C. Li, Potential 2D thermoelectric material ATeI (A = Sb and Bi) monolayers from a first-principles study, *Nanotechnology*, 2017, **28**(44), 445702.
69 E. Bolen, E. Deligoz and H. Ozisik, Origin of low thermal conductivity in monolayer PbI_2, *Solid State Commun.*, 2021, **327**, 114223.
70 L. Li, *et al.*, Theoretical analysis of the thermoelectric properties of penta-PdX_2 (X = Se, Te) monolayer, *Front. Chem.*, 2022, **10**, 1061703.
71 D. Wan, *et al.*, Anharmonicity and weak bonding-driven extraordinary thermoelectric performance in wrinkled SnSe monolayer with low lattice thermal conductivity, *Ceram. Int.*, 2024, **50**(6), 9591–9603.
72 G. Liu, *et al.*, First-principles study of lattice thermal conductivity of Td–WTe_2, *New J. Phys.*, 2016, **18**(3), 033017.
73 N. K. Sharma, *et al.*, Ultralow thermal conductivity of W-Janus bilayers (WXY: X, Y = S, Se, and Te) for thermoelectric devices, *Nanoscale*, 2024, **16**(6), 3091–3100.
74 E. A. Moujaes and W. Diery, Thermoelectric properties of 1 T monolayer pristine and Janus Pd dichalcogenides, *J. Phys.: Condens. Matter*, 2019, **31**(45), 455502.
75 G. Xie, D. Ding and G. Zhang, Phonon coherence and its effect on thermal conductivity of nanostructures, *Adv. Phys.:X*, 2018, **3**(1), 1480417.

© 2025 The Author(s). Published by the Royal Society of Chemistry

Open Access Article. Published on 24 December 2024. Downloaded on 2/15/2026 7:07:25 PM.
This article is licensed under a Creative Commons Attribution-NonCommercial 3.0 Unported Licence.

76 N. Mounet and N. Marzari, First-principles determination of the structural, vibrational and thermodynamic properties of diamond, graphite, and derivatives, *Phys. Rev. B: Condens. Matter Mater. Phys.*, 2005, **71**(20), 205214.
77 Z. Zhou, *et al.*, High thermoelectric performance originating from the grooved bands in the $ZrSe_3$ monolayer, *ACS Appl. Mater. Interfaces*, 2018, **10**(43), 37031–37037.
78 N. Stojanovic, *et al.*, Thermal conductivity in metallic nanostructures at high temperature: Electrons, phonons, and the Wiedemann-Franz law, *Phys. Rev. B: Condens. Matter Mater. Phys.*, 2010, **82**(7), 075418.
79 V. Van Thanh and N. T. Hung, Janus 2D B2P6: A promising anisotropic thermoelectric material with high power factor, *Surf. Interfaces*, 2024, **44**, 103829.
80 W. Hussain, *et al.*, Advances in nanoparticle-enhanced thermoelectric materials from synthesis to energy harvesting: A review, *ACS Omega*, 2024, **9**(10), 11081–11109.
81 G. J. Snyder and T. S. Ursell, Thermoelectric efficiency and compatibility, *Phys. Rev. Lett.*, 2003, **91**(14), 148301.
82 D. Luo, *et al.*, Realizing ultrahigh ZT value and efficiency of the Bi_2Te_3 thermoelectric module by periodic heating, *Energy Convers. Manage.*, 2023, **296**, 117669.
83 M. A. Mohebpour, *et al.*, Thermoelectric characteristics of X_2YH_2 monolayers (X = Si, Ge; Y = P, As, Sb, Bi): a first-principles study, *Sci. Rep.*, 2021, **11**(1), 23840.
84 K. Sujata, *et al.*, Two-dimensional $BiSbTeX_2$ (X = S, Se, Te) and their Janus monolayers as efficient thermoelectric materials, *Phys. Chem. Chem. Phys.*, 2024, **26**(42), 27163–27175.
85 N. T. Hung, A. R. Nugraha and R. Saito, Designing high-performance thermoelectrics in two-dimensional tetradymites, *Nano Energy*, 2019, **58**, 743–749.
86 S.-H. Cao, *et al.*, Electronic and thermoelectric properties of semiconducting Bi_2SSe_2 and Bi_2S_2Se monolayers with high optical absorption, *Phys. Chem. Chem. Phys.*, 2022, **24**(43), 26753–26763.
87 M. Ould-Mohamed, *et al.*, Janus $ScYCBr_2$ MXene as a Promising Thermoelectric Material, *ACS Appl. Energy Mater.*, 2024, **7**(15), 6598–6611.
88 Z. Zhou, *et al.*, Anomalous Thermoelectric Performance in Asymmetric Dirac Semimetal BaAgBi, *J. Phys. Chem. Lett.*, 2022, **13**(10), 2291–2298.
89 Z. Shu, *et al.*, High-performance thermoelectric monolayer γ-GeSe and its group-IV monochalcogenide isostructural family, *Chem. Eng. J.*, 2023, **454**, 140242.